Razzaq, M.Y.; Behl, M.; Noechel, U.; Lendlein, A.:

Magnetically controlled shape-memory effects of hybrid nanocomposites from oligo(Omega-pentadecalactone) and covalently integrated magnetite nanoparticles

In: Polymer (2014) Elsevier

DOI: 10.1016/j.polymer.2014.07.025

Magnetically Controlled Shape-Memory Effects of Hybrid Nanocomposites from Oligo(*ω*-pentadecalactone) and Covalently Integrated Magnetite Nanoparticles

Muhammad Yasar Razzaq, Marc Behl, Ulrich Nöchel, Andreas Lendlein*

Institute of Biomaterial Science and Berlin-Brandenburg Center for Regenerative Therapies, Helmholtz-Zentrum Geesthacht, Kantstrasse 55, 14513 Teltow, Germany

*To whom correspondence should be addressed
E-mail: andreas.lendlein@hzg.de

Keywords: magnetite nanoparticles, hybrid nanocomposites, shape-memory polymers, magnetic nanoparticle netpoints

Abstract

The covalent integration of inorganic nanoparticles in polymer matrices has gained significance for improving the structural properties of polymer-based materials. Here we report on the performance of poly(*ω*-pentadecalactone) networks with magnetite nanoparticles as netpoints in their magnetically-controlled shape-memory capability. Hybrid nanocomposites with magnetite nanoparticle content ranging from 5 to 11 wt% were prepared by reacting two types of oligo(*ω*-pentadecalactone) (OPDL) based precursors with terminal hydroxy groups, a three arm OPDL (^{3}AOPDL, M_n = 6000 g·mol^{-1}) and an OPDL (M_n = 3300 g·mol^{-1}) coated magnetite nanoparticles (∅ = 10 nm), with a diisocyanate. Homogenous hybrid nanocomposites were obtained

independent from the weight content of the OPDL decorated nanoparticles in the samples. At 100 °C ($T > T_{m\text{-}OPDL}$) the covalent integration of the nanoparticles increased the mechanical strength with increasing weight content whereby the elasticity remained almost constant. In magnetically-controlled one-way dual-shape experiments the shape fixity decreased from 95% to 90% but the shape recovery increased slightly from 95% to 97% when the nanoparticle content was increased. In magnetically-controlled reversible dual-shape experiments the nanoparticles had a restraining effect and the maximum shape-change of 65% for hybrid nanocomposites with 5 wt% magnetite nanoparticles was reduced to 36% when the particle content was increased to 11 wt%. These results show that the performance of hybrid nanocomposites can be tailored by nanoparticle content, however in terms of their applicability either mechanical strength or actuation capability should be focussed in the material selection.

1. Introduction

Multimaterial systems received significant interest in material research as novel functions such as electrical conductivity or sensitivity towards magnetic fields can be implemented into the material by the additional material component.[1-5] Composites are here of particular interest as in general the additional material component can be integrated by blending of the (in)organic particulate filler with the polymer matrix.[6-11] Compared to blending, the covalent integration of the particulate component can substantially enhance e.g. the structural function of the resulting hybrid composites as the filler becomes an integral part of the polymer network.[12-18] The covalent integration of magnetite nanoparticles (MNP) in hybrid nanocomposites (H-NC) based on oligo(ω-pentadecalactone) (OPDL) enabled reversibility of a magnetically controlled dual-shape effect (R_{mag}-DSE).[19]

Materials capable of such a reversible shape-memory effect (R-SME) can shift between two memorized shapes i.e., upon heating they deform to one shape and change to another shape when cooled.[20-26] This R-SME is based on the reversible actuation of semicrystalline polymer networks at a constant external stress (σ_{const}). In contrast, in polymers providing a one-way shape-memory effect (1W-SME), only the recovery step is spontaneous upon stimulation and an external mechanical manipulation is always required to obtain the temporary shape again.[27-34]

The reversibility of the SME in hybrid nanocomposites could be achieved as the covalent integration of MNP enabled a uniform distribution of MNP and in this way a higher temperature could be reached when exposed to an alternating magnetic field (AMF) as compared to a reference composite prepared by physically mixing the MNP with the polymer. In addition, by the covalent integration of MNP they became multifunctional netpoints of the polymer network and by this contribute to the structural integrity of the H-NC once the melting temperature of the polymer chain segments is exceeded. A covalent integration of the MNP in SMPs was investigated by ring-opening metathesis polymerization of norbornene adsorbed on the surface of MNP by carboxylic acid groups.[35] Norbornene was selected as the bulky groups prevent the MNP aggregation and further help to covalently integrate MNP by way of copolymerization. However, these composites could not withstand a temperature above 80-100 °C and were melted indicating the failure of MNP crosslink at this temperature range.

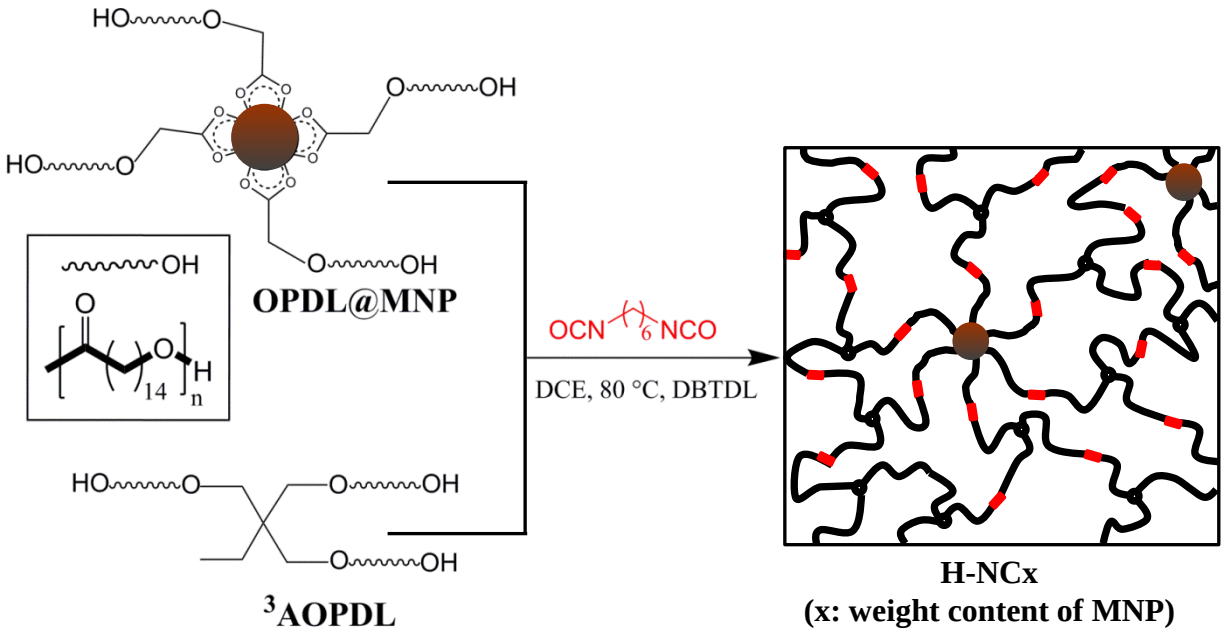

Figure 1. Synthesis and crosslinking of precursors ^{3}AOPDL and OPDL@MNP using Bu_2SnO and DBTDL as catalysts and DCE as a solvent.

Here, we explored the performance of H-NCs in magnetically controlled one-way and reversible SMEs. Emphasis of this study is given to the recoverability of the original shape and of the shape change in the reversible SME. Key requirements for materials capable of a SME is a polymer architecture consisting of netpoints determining the permanent shape and polymer chain segments interconnecting the netpoints, which in case of a 1W-SME act as reversible crosslinks by solidification (e.g. melting and crystallization). The netpoints determine the shape stability and by this the shape recovery. In addition, the H-NC need to provide a certain degree of elasticity at a high temperature (T_{high}) above the melting temperature (T_m) of the switching domains to enable programming of the temporary shape by deformation to an elongation ε_m, which afterwards can be fixed by subsequent cooling. In case of a R-SME, the polymer chain segments must be capable to actuate the material while a constant stress (σ_{const}) is applied to the

H-NC by a directed crystallization-induced elongation (CIE) when cooled to a low temperature (T_{low}) ($T_{low} < T_m$), which can be reversed by a melting-induced contraction (MIC).[22, 36-39] Here for the sake of practicability, a T_m and crystallization temperature (T_c) well-above room temperature is preferable. These thermal requirements of the H-NCs can be fulfilled by cyrstallizable OPDL switching segments. The H-NCs were synthesized by crosslinking of hydroxyl terminated ^{3}AOPDL and OPDL@MNP with 1,6-hexane diisocyanate (HDI) in a polyaddition reaction catalyzed by dibutyltin dilaurate (DBTDL) (Figure 1). To achieve a magnetic control by indirectly triggering a thermally-induced effect, the amount of MNP should be high enough to enable a $T_{max} > T_{m\text{-}OPDL}$ upon exposure to AMF. Therefore, the amount of OPDL@MNP was varied between 17 wt% and 30 wt% resulting in H-NC with a MNP content between 5 and 11 wt%. In such H-NC the OPDL@MNPs are acting as novel nanoparticulate crosslinks, which on the one hand enable an indirectly triggered thermally-induced SME but on the other hand influence netpoint density as well as crystallization behavior of the OPDL chain segments. Therefore the influence of OPDL@MNP on the thermal and mechanical properties as well as in specifically designed magneto-mechanical experiments on the 1W_{mag}-DSE and R_{mag}-DSE is investigated. Here in particular the role of the OPDL@MNP on T_m and T_c as well as on the shape recovery (R_r) will be explored. The influence of the OPDL@MNP on the crystallization behavior was studied by wide angle X-ray scattering (WAXS) analysis to correlate the microstructural changes during R-DSE with the morphology of the H-NC and by this elucidate design principles for better performance of the H-NCs.

2. Experimental part

2.1. Materials

ω-pentadecalactone (PDL), dibutyltin dilaurate (DBTDL), 1,6-hexane diisocyanate (HDI), and dichloroethane were of analytical grade (Sigma-Aldrich Munich, Germany) and were used as received.

2.2. Synthesis of hybrid nanocomposites

The synthesis of H-NCs was carried out according to the reported procedure.[19] For the synthesis of H-NC9, 0.7 g **(**0.021 mmol of hydroxyl groups) of OPDL@MNP ($M_n \approx 3300$ g·mol^{-1} of OPDL chains determined by GPC) and 2.3 g (0.4 mmol) of ^{3}AOPDL ($M_n \approx 6{,}000$ g·mol^{-1} determined by GPC) were sonicated in 10 mL dichloroethane (DCE) for 10 min. Afterwards, 0.17 mL (1.1 mmol) HDI and 3 µL (0.005 mmol) DBTL were added. The reaction mixture was stirred vigorously at 200 rpm (Heidolph, RZR2102, Schwabach, Germany) for one hour, subsequently poured into a Teflon dish, which was kept at 80 °C for 24 h under a constant nitrogen flow then four days at 100 mbar. The nanocomposite was purified three times by extraction with chloroform and subsequent drying. The nomenclature of the composites is given as H-NCx, where x is the amount of MNP determined by thermogravimetric analysis (TGA) whereas the homonetworks obtained by crosslinking pure ^{3}AOPDL were named as N-^{3}AOPDL.

2.3. Characterization methods

The OH-numbers of the ^{3}AOPDL and OPDL@MNP precursors were determined with a 716 DMS/719 S Titrino titrator system in combination with a LiCl-electrode (Metrohm, Filderstadt, Germany). M_n of the ^{3}AOPDL and of the OPDL chains degrafted from MNP were determined by a multidetector GPC-system consisting of two 300 mm x 8.0 mm linear M columns (Polymer

Standard Service, Mainz, Germany), an isocratic pump 2080 and an automatic injector AS 2050 (both Jasco, Groß-Umstadt, Germany), a RI detector Shodex RI-101 (Showa Denko Europe, Munich, Germany), and a differential viscometer/light scattering dual detector T60A (Viscotek Europe, Crowthorne, UK) using chloroform as eluent at 35 °C with a flow rate of 1.0 $mL \cdot min^{-1}$, and 0.2 wt% toluene as internal standard.

Gel content (G) and degree of swelling (Q) were determined by swelling the films in a 100-fold excess (related to the sample weight) of chloroform overnight and subsequent drying at room temperature. Endpoints of swelling and drying were reached when the weight remained constant. The gel content G was calculated as the ratio of the non-swollen (m_0), and the extracted mass (m_{ex}) determined from swelling experiments according to equation 1.

$$G = \frac{m_{ex}}{m_o} \cdot 100\% \tag{1}$$

The volumetric degree of swelling Q_v in chloroform was calculated according to Equation 2:

$$Q_v = 1 + \rho_2 \cdot \left(\frac{m_{sw}}{m_{ex} \cdot \rho_1} - \frac{1}{\rho_1} \right) \tag{2}$$

The mass of the sample in the swollen state is described by m_{sw}, ρ_1 describes the density of the swelling medium (chloroform), and ρ_2 the density of the dry polymer network. The density ρ_2 was determined with an Ultra Pycnometer (Quantachrome, Odelzhausen, Germany) at 25 °C using a measurement cell with a calibration volume of 1.0725 cm^3.

Scanning electron microscopy (SEM) was performed using a Zeiss Gemini, Supra 40VP (Zeiss, Jena Germany) at an accelerating voltage of 10 kV. Ultrathin sections of 70 nm were cut on a Leica FC6 cryo ultra-microtome at 130 °C (Leica Microsystems GmbH Wetzlar, Germany). Morphology of the nanocomposites was determined by Transmission Electron Microscopy

(TEM) with a Zeiss EM 902 (Zeiss, Oberkochen, Germany). DSC experiments were performed with a Netzsch (Selb, Germany) DSC 204, in the temperature range from -100 to 100 °C with a constant heating and cooling rate of 5 $K \cdot min^{-1}$ under nitrogen environment. Wide angle X-ray scattering (WAXS) measurements were performed on an X-ray diffraction system Bruker D8 Discover with a two dimensional detector from Bruker AXS (Karlsruhe, Germany).

Optical polarization microscopy was performed on a Zeiss Axio Imager A1m microscope (Carl Zeiss, Jena, Germany) equipped with crossed polarizers and a Linkam LTS 350 heating stage (Linkam Scientific Instruments Ltd., Tadworth, United Kingdom). A 20x magnification was used in transmission mode.

Inductive-heating of H-NC was accomplished by positioning the sample in an alternating magnetic field at a frequency of f = 258 kHz. By adjusting the generator (TIG 5/300 high-frequency generator, Huettinger Electronic; Freiburg, Germany) power output, the magnetic field strength in the center of the coil could be varied between 7 and 30 $kA \cdot m^{-1}$. Magneto-mechanical experiments were conducted in a setup combining the high-frequency generator and the copper inductive coil with a tensile tester (Zwick Z2.5 Ulm, Germany). The nanocomposite samples were fixed in the center of the inductor coil with the help of plastic clamps.

2.4. Magnetomechanical Investigations

Investigation of 1W_{mag}-DSE: The H-NC were magnetically heated for 5 min at a high magnetic field strength (H_{high}), causing a T_{max} of 100 °C followed by application of an external stress resulting in a deformation ε_m = 50%. The ε_m was kept constant when the magnetic field was switched off (H_{low} = 0) so that the sample temperature decreased to ambient temperature. Subsequently the stress was released resulting in the temporary shape of the sample at strain ε_u.

Finally, the shape recovery to ε_p was observed by indirectly reheating the sample at H_{high} for five minutes under stress-free conditions. Each experiment consisted of four cycles, where the first cycle was used as a preconditioning step. From each cycle the shape-fixity ratio (R_f) and R_r were calculated.

Investigation of R_{mag}-DSE: The samples were deformed to ε_m = 50% under strain-controlled conditions, this deformation was kept for 5 min afterwards σ was determined. Then the tensile tester was switched to stress control mode and the determined stress as applied as σ_{const}, which was kept constant resulting in shape B (ε_{rev}). In the magneto-mechanical cycle, H was decreased from H_{high} to H_{low} under σ_{const}, whereby the sample elongated to shape A (ε_{act}). H was kept constant for 5 min for equilibration. Subsequent increase of H from H_{low} to H_{high} resulted in a contraction of the sample to shape B´ (ε_{rev}) again. The cyclic, magneto-mechanical experiments were carried out by using σ_{const} = 1.2 MPa for H-NC5, 0.8 MPa for H-NC9, and σ_{const} = 0.7 MPa for H-NC11. At each σ_{const}, the cycle was repeated three times. This R_{mag}-DSE was quantified by the relative increase in strain $R_{act,H}$(N) for the Nth cycle given by the ratio of the sample dimensions at H_{low} minus the sample dimension at H_{high} and sample dimension at H_{high}.

$$R_{\mathrm{act,H}}(\mathrm{N}) = \frac{\varepsilon_{act(N)H_{low}} - \varepsilon_{rev(N-1)H_{high}}}{\varepsilon_{rev(N-1)H_{high}}} \quad (3)$$

After actuation because of CIE, the percentage of the shape recovery which took place by MIC at H_{high} was determined by measuring the value of $R_{r,H}$(N) for the Nth cycle as follow

$$R_{\mathrm{r,H}}(\mathrm{N}) = \frac{\varepsilon_{act(N)H_{low}} - \varepsilon_{rev(N)H_{high}}}{\varepsilon_{act(N)H_{low}} - \varepsilon_{rev(N-1)H_{high}}} \quad (4)$$

The value of σ_{const} was kept constant during actuation and recovery.[19]

3 Results and discussion

3.1. Morphology and thermal analysis of the hybrid nanocomposites

The gel contents (*G*) of the polymer networks and hybrid composites ranged between 90% and 98% indicating an almost complete crosslinking reaction and were independent from the OPDL@MNP content. The covalent attachment of the MNP prevented leaching of the particles during swelling. With increasing content of OPDL@MNP, the degree of swelling (*Q*) was decreased indicating an increase in crosslinking density. The value of Q = 520% was maximum for N-^{3}AOPDL, while the sample with the highest amount of OPDL@MNP had the lowest value of Q = 280% (Table 1) and was attributed to the higher netpoint functionality of the coated nanoparticles. The integration of MNP in terms of distribution within the nanocomposites as a function of MNP content was investigated by SEM and is shown exemplarily for the sample with the highest MNP content in Figure 1a. The obtained SEM images from the H-NC samples showed homogeneously distributed MNP in the polymer matrix, with a uniform concentration throughout the bulk of the sample. In addition, large agglomerates, as found in the case of physically incorporated MNP nanocomposites,[19] were not observed in the SEM images of these samples. For H-NC5 only few aggregates with a size in the range between 50 nm and 100 nm were found while the size of these clusters was increased by increasing the OPDL@MNP content in the reaction mixture *e.g.* for H-NC11 the cluster size was increased to 2-3 μm (Figure 2a). Nevertheless an efficient dispersion of the MNP in polymer matrix could be assumed as no sedimentation of the heavier particles during solvent evaporation was monitored. Only few aggregates with a size in the range between 50 nm and 100 nm were found so that an efficient dispersion of the MNP in polymer matrix can be assumed. The nanostructure of the H-NC samples was investigated by transmission electron microscopy (TEM) analysis to further prove

the homogenous distribution of the MNP (Fig. 2b). Again, an efficient dispersion of the MNP (10-12 nm) in the nanocomposite was observed and was attributed to the covalent integration of the OPDL@MNP in the polymer network. WAXS measurements, which were performed at three different loactions of the samples, revealed a homogenous distribution of crystallinity. While for H-NCs with a MNP content < 5 wt% a nucleation the MNP was determined,[19] this effect could not be observed in H-NCs with higher MNP contents. Here a reduction of crystallinity was found.

Optical polarization microscopy (POM) with crossed polarizers was performed on H-NCs at room temperature and is exemplary shown for H-NC11 in the isotropic state (Figure 2-c). Here only crystalline regions transmit a light signal resulting in a bright spot on the POM-image. The MNP netpoints do not transmit the light. The sample exhibited relatively random distributed crystalline regions as reflected by the bright spots of the POM image. When the sample was heated to 100 °C no bright spots were observed as the polymer chain segments became amorphous. Furthermore, a potential crystallization in the vicinity of the MNP indicating a nucleation effect of the MNP was not observed.

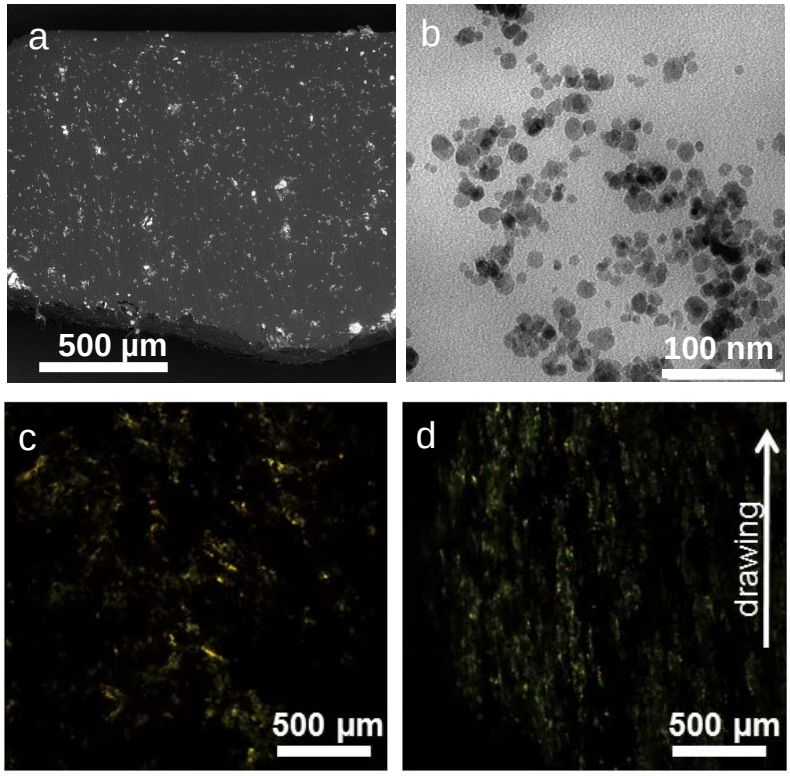

Figure 2. a) SEM image of H-NC11. b) TEM image of H-NC11. c) POM image of non-deformed H-NC11. d) POM image of H-NC11 after programming to 50% elongation.

Table 1: Thermal and morphological properties of the composites.

Sample ID	μ_{MNP} (%)[a)]	G (%)[b)]	Q (%)[c)]	T_m (°C)[d)]	ΔH_m ($J \cdot g^{-1}$)[e)]	T_c (°C)[f)]	DOC (%)[g)]
N-^{3}AOPDL	0	98 ± 1	520 ± 25	73 ± 1	81 ± 1	50 ± 1	28 ± 1
H-NC5	5 ± 1	95 ± 1	370 ± 30	74 ± 1	87 ± 1	56 ± 1	31 ± 1
H-NC9	9 ± 1	90 ± 1	340 ± 15	77 ± 1	94 ± 1	61 ± 1	26 ± 1
H-NC11	11 ± 1	97 ± 1	280 ± 10	80 ± 1	91 ± 1	64 ± 1	23 ± 2

[a)] MNP content determined by TGA [b)] gel content [c)] degree of swelling [d)] melting temperature determined by DSC [e)] melting enthalpy determined by DSC [f)] crystallization temperature determined by DSC [g)] degree of crystallinity determined by WAXS measurements.

The influence of the OPDL@MNP on the thermal properties of composites was examined by means of DSC. In Figure 1b the thermograms of the second heating run with the corresponding

melting peaks are shown while the thermal transition temperatures and the melting enthalpies of the samples are summarized in Table 1. The T_m and T_c of the nanocomposites increased modestly along with their associated latent heat of melting and crystallization, with increasing OPDL@MNP content from 0 to 30 wt%. T_c increased from 50 °C for N-^{3}AOPDL to 64 °C for H-NC11 while T_m increased from 73 °C for N-^{3}AOPDL to 80 °C for H-NC11 (Table 1) and can be explained by a better heat distribution of the MNP in cooling direction resulting crystallization at higher temperatures while in heating direction the heat distributing effect of the MNP is less pronounced due to the crystalline OPDL domains. As T_c and T_m increase both it is assumed that the MNP cause crystalline domains of a more uniform crystallinity. Nevertheless, the transition temperatures required for tailoring the shape-memory properties can be tuned by changing the OPDL@MNP content in H-NCs. Furthermore, the necessary condition of these nanocomposites providing a T_m sufficiently above the room temperature for 1W_{mag}-DSE and R_{mag}-DSE can be accessed from the thermograms.

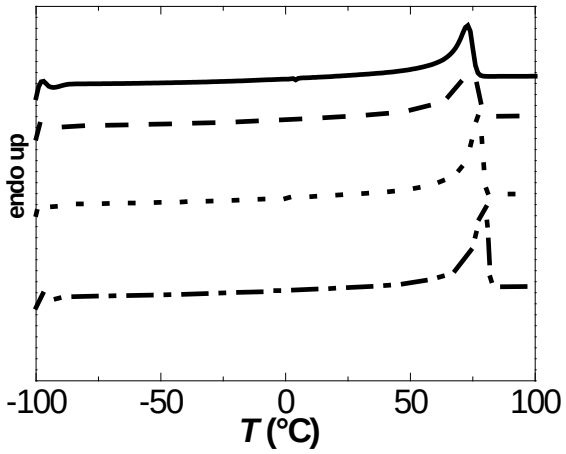

Figure 3. DSC thermograms of H-NC (N-^{3}AOPDL: black line, H-NC5: dashed line, H-NC9: dotted line, H-NC11: dashed-dotted line.

On the basis of the thermal transitions in these composites, a T_{high} = 100 °C, which is well above the $T_{m,OPDL}$ and a T_{low} = ambient temperature (T_{amb}) was selected for the magneto-mechanical experiments to demonstrate the 1W_{mag}-DSE and the R_{mag}-DSE.

3.2. Mechanical properties of the composites

An initial deformation of ε_m = 50% was selected to ensure an orientation of the OPDL chain segments required for the CIE of a R_{mag}-SME but to keep at the same time the samples within the geometrical boundaries of the inductor coil from the experimental setup consisting of the frequency generator and the inductor coil placed within the tensile tester. Therefore, an elongation at break ε_b > 50% at T_{high} = 100 °C was required for these samples. The elastic properties of N-^{3}AOPDL and nanocomposites were examined in uniaxial tensile tests at 25 °C and 100 °C. The obtained elastic modulus (E), maximum stress (σ_{max}), and ε_b are summarized in Table 2. In H-NCs, which have covalently crosslinked MNP, the value of ε_b was gradually decreased with increasing amount of OPDL@MNP in the reaction mixture.

Table 2: Mechanical properties of the N-^{3}AOPDL and the composites.

	25 °C			100 °C		
Sample ID	E (MPa)[a)]	σ_{max} (MPa)[b)]	ε_b (%)[c)]	E (MPa)[a)]	σ_{max} (MPa)[b)]	ε_b (%)[c)]
N-^{3}AOPDL	121 ± 21	25 ± 2	500 ± 20	2.8 ± 0.2	1.0 ± 0.5	60 ± 10
H-NC5	33 ± 7	9 ± 2	280 ± 20	3.5 ± 0.3	1.3 ± 0.1	70 ± 2
H-NC9	155 ± 20	10 ± 2	220 ± 40	3.6 ± 0.2	1.5 ± 0.2	80 ± 12
H-NC11	135 ± 6	14 ± 1	155 ± 5	5.1 ± 0.2	2.1 ± 0.2	70 ± 10

[a)] Elastic modulus, [b)] maximum stress, and [c)] elongation at break determined by tensile tests.

At 25 °C, the maximum value of ε_b = 500% was observed for N-^{3}AOPDL and decreased to ε_b = 155% for H-NC11, which can be explained by the increase in crosslink density when the

OPDL@MNP content was increased. However, no systematic correlation was observed for *E* with values between 33 MPa and 155 MPa, which might be attributed to some antagonistic effects of the MNP in terms of increase in crosslink density and decrease of crytsallinity. At 100 °C, an increasing trend in *E* by increasing OPDL@MNP content in H-NC was observed. The value of *E* was increased from 2.8 MPa for N-^{3}AOPDL to 5.1 MPa for H-NC11 and can be attributed to the increase in crosslink density (υ_c). By applying the Mooney-Rivilin equation [40, 41] an increase of υ_c from 4.3×10^{-4} mol·cm^{-3} for N-^{3}AOPDL to 5.4×10^{-4} mol·cm^{-3} for H-NC11 was quantified. At 100 °C ε_b values ranged from 60% to 80%. Also at 100 °C a slight increase in σ_{max} was observed when the OPDL@MNP content was increased. The mechanical analysis particularly at 100 °C indicate that OPDL@MNP provides chemical crosslinks and act as reinforcing filler with homogenous distribution of MNP.

3.3. Magneto-mechanical experiments for 1W_{mag}-DSE and R_{mag}-DSE

1W_{mag}-DSE and R_{mag}-DSE were investigated in a setup consisting of an inductor coil equipped with a tensile tester.[19] Despite the increase in surface to volume ratio upon deformation, which goes along with a lowering of the maximum bulk temperature that can be reached the H-NC could be deformed to elongations larger than 50% and were able to reach a T_{max} ~ 100 °C by exposure to AMF.[42] 1W_{mag}-DSE was investigated for the H-NCs containing 5 to 11 wt% of MNP in cyclic, magneto-mechanical experiments. Here, each cycle consists of heating and equilibration of the composites at H_{high} to enable a T_{max} = 100 °C well above the $T_{m\text{-}OPDL}$. H_{high} was varied for different samples depending on the weight content of MNP *e.g.* H_{high} = 18.2 kA·m^{-1} for H-NC5, H_{high} = 17 kA·m^{-1} for H-NC9, and H_{high} = 15.4 kA·m^{-1} for H-NC11 were used as the heating capacity of the composites is a function of the weight content of MNP. The

magnetic heating was followed by an elongation to ε_m = 50% for all samples to keep them within the geometrical boundaries of the magnetic coil. The temporary shape was fixed by switching off the magnetic field to H_{low} = 0 kA·m^{-1} and cooling the composites to T_{amb}. Subsequently, the recovery of the composites was observed under-stress free conditions by switching the field strength to H_{high}. The curves of the elongation recorded during programming and recovery of the H-NC9 and H-NC11 is exemplarily shown in Figure 4a. All nanocomposites displayed a very fast recovery (≈ 3 min) to ε_p with a $R_r \geq 95\%$ (Table 2). The fast recovery of the nanocomposites was attributed to an increased transfer of heat from bulk of the material to the surface due to the inductive heating of MNP loading. In contrast to the previous investigations in which the particles were non-covalently integrated, [43] R_r was slightly increased by increasing the MNP netpoints and a maximum value of R_r = 97% was observed for H-NC11 with maximum amount of MNP. This can be attributed to the increased crosslinking density when the wt% of MNP was increased. However, the value of R_f was gradually decreased when the netpoint density provided by the MNP was increased and a value of R_f = 90% was achieved for the samples with maximum amount of MNP netpoints (Table 2) and might be attributed to a hindered crystallization of oriented polymer chain segments at higher MNP content. In addition, no significant change in the R_r or R_f was observed with raised number of cycles.

To enable the R_{mag}-DSE, deformation at H_{high} was carried out under stress-controlled mode of the tensile tester. An initial stress σ_{const} of 0.8 MPa was applied for H-NC9 to achieve the required deformation of ε_m = 50%. The applied stress was kept constant and a surface temperature of 92 °C was recorded after elongation. Once the magnetic field was switched to H_{low} = 0, the cooling took place and the sample elongated quite dramatically at the beginning of crystallization from ε_m to ε_{act} ≈ 73% in the direction of applied stress. The effect was reversible and after

applying H_{high} = 17 kA·m^{-1} the sample contracted back to the original strain ε_{rev} (Figure 3b). Heating the nanocomposite above the $T_{m,OPDL}$ by applying H_{high} reversed this elongation as the directed polymer chain segments recoil entropy driven until the applied stress is balanced.[44, 45] Under constant σ_{const}, these elongation and contraction steps were repeatable and could be controlled by AMF. For the H-NC11, σ_{const} of 0.7 MPa was used to stretch the samples to ε_m = 50%.

a) b)

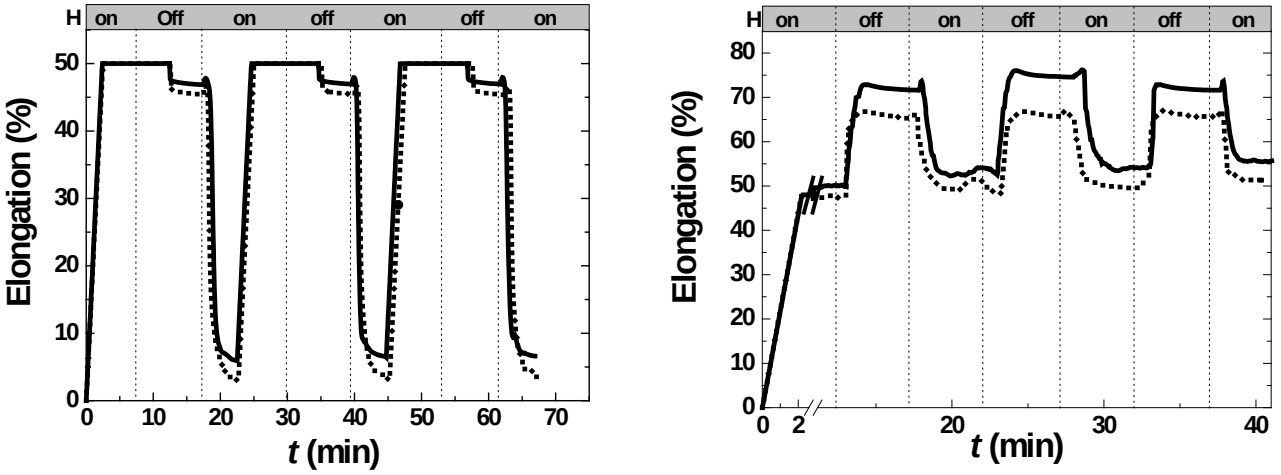

Figure 4. a) 1W_{mag}-DSE b) R_{mag}-DSE in H-NCs with different amount of MNP content. Black line: solid line H-NC9 (H_{high} = 17 kA·m^{-1}), dotted line H-NC11 (H_{high} = 15.4kA·m^{-1}).

Lower H_{high} values could be used to achieve the T_{max} = 100 °C. The similar R_{mag}-DSE with relatively lower values of ε_{act} = 66% was achieved for H-NC11 as shown in Figure 4b. This R_{mag}-DSE was quantified by determining the relative increase in strain ($R_{act,H}$) between the sample dimension at H_{low} and the sample dimension at H_{high}. The R_{mag}-DSE was quantified by determining the relative increase in strain ($R_{act,H}$) at H_{low} and the percentage of recovery ($R_{r,H}$) at

H_{high} (see experimental part 2.4 for further information).[19] For H-NC5, an average $R_{act,H}$ of 65±3% and an average $R_{r,H}$ of 95±3% was determined for three cycles.[19] By increasing the MNP netpoints in H-NCs, the actuation due to CIE was decreased. The value of $R_{act,H}$ was decreased to 43±2% for H-NC9 and to 36±2% for H-NC11. This can be attributed to the MNP crosslinks, which impose a constraint against the deformation of the nanocomposite during CIE and result a decrease of aligned crystal formation during CIE. Nevertheless, $R_{r,H}$ > 92% was achieved for both samples. At the same time, no significant change in the value of $R_{act,H}$ was observed for all samples by increasing the magnetically-controlled number of cycles. This indicated that no breakage of the covalent bonds took place during R_{mag}-DSE, which would decrease orientation and in this way $R_{act,H}$.

Table 3: Shape-memory properties of the composite

Sample ID	R_f [%]	R_r [%]	$R_{act,H}$	$R_{r,H}$
H-NC5	95 ± 0.2	95 ± 1	66 ± 2	96 ± 2
H-NC9	94 ± 0.1	95 ± 1	43 ± 2	90 ± 2
H-NC11	90 ± 0.0	97 ± 1	36 ± 2	94 ± 2

3.4. Investigation of the Influence of the MNP on Morphology by X-Ray Analysis

In order to analyze the influence of the OPDL@MNP content during R_{mag}-DSE, WAXS measurements were conducted with H-NCs in analogy to the magneto-mechanical experiments by application of external heating of T_{high} = 100 °C at σ_{const} from 0.1 to 0.6 MPa and cooling to $T_{low} = T_{amb}$ at σ_{const}. Scattering patterns were recorded at T_{amb} after actuation of HNCs (at T_{high} = 100 °C the OPDL was amorphous and exhibited no crystalline reflections).

Figure 4 shows the azimuthal profiles (I vs χ) of the (110)-reflection of crystalline OPDL in H-NCs under mechanical load in the second actuation cycle of R_{mag}-DSE. The shape (i.e. the sharpness) of the profile is related to the degree of orientation of the (110)-symmetry plane and thus to the crystal orientation in the specimen. In H-NC5 (Figure 5a) with σ_{const} = 0.1 and 0.2 MPa only a slight orientation was observed, which was related to the small reversible actuation as obtained by tensile experiments. Once 0.4 MPa was imposed to the sample, the degree of orientation increased significantly and the azimuthal profile became more pronounced.

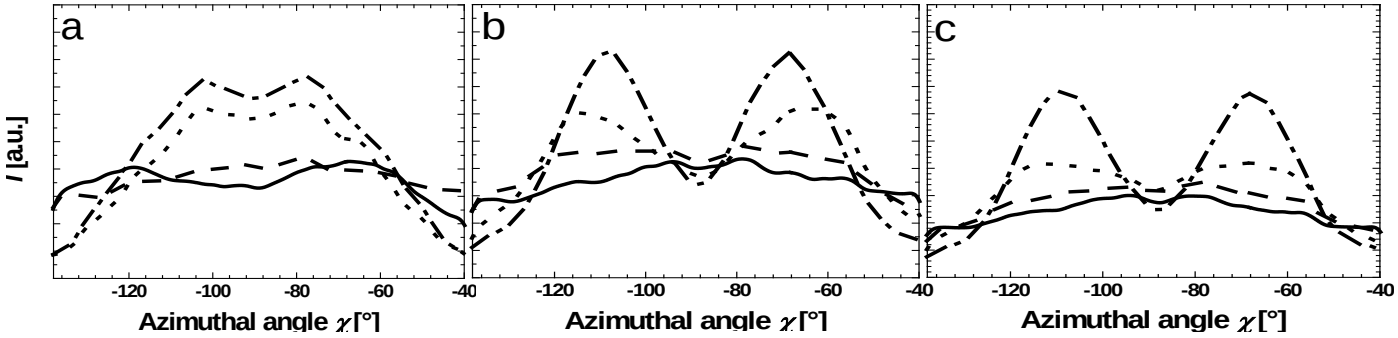

Figure 5: Azimuthal profiles of the OPDL (110)-reflection of H-NC5 (a), H-NC9 (b), and H-NC11 (c) during R_{mag}-DSE with σ_{const} = 0.1 (solid line), σ_{const} = 0.2 (dashed line), σ_{cons} = 0.4 (dotted line), and σ_{const} = 0.6 MPa (dash-dotted line).

This behavior correlated with the increased reversible actuation strain observed in uniaxial tensile tests. For 0.6 MPa the sharpness of the peak profile was even increased as well as the actuation. For H-NC9 (Figure 5b), only a slight crystal orientation was observed when 0.1 and 0.2 MPa were applied as reflected by the relative flat azimuthal profiles of the OPDL (110)-reflection. This observation correlated to the low actuation strain during tensile measurements when a magnetic field was applied. When the mechanical load was increased to 0.4 MPa an abrupt change in the peak profile was observed. On one hand the crystal orientation increased as

reflected by the non-flat profile, on the other hand the profile differed from the neat PPDL-profile at this stress as the intensity distribution became bimodal. Two peak maxima at χ ~ -115° and -67° were determined, which correspond to a tilt angle of ~25° (in χ) related to the equator (drawing direction being the meridian). The bimodal peak can be attributed to a structure of tilted crystals having an inclination of the molecular axis of ~25° to the left and right of the meridian. Similar observations are reported for polyethylene.[20] When the stress was increased to 0.6 MPa the peak profile increased in sharpness and the bimodal character was maintained. For H-NC11 (Figure 5c) the peak profile also became bimodal for increased σ_{const} (e.g. 0.4 and 0.6 MPa). These results of a directed crystallization correlate with the findings from POM investigations in which a H-NC-5 sample was heated to 100 °C, a deformation of ε = 50% was applied, which was afterwards fixed by cooling to 25 °C and subsequently the POM image shown was recorded (Figure 2-d). Here the drawing direction is vertical as indicated by an arrow. The crystalline structure presented distinct alignment along the drawing direction with a homogenous distribution of the light scattered signals.

Nonetheless, the sharpness of the profiles in the WAXS profiles decreased with fixed σ_{const} = 0.6 MPa in the order H-NC5 > H-NC9 > H-NC11, which can be attributed to the decreased orientation. Summarizing the WAXS investigations, it can be said that the reversible length changes can be explained by a directed crystallization of the polymer chain segments forming lamellae perpendicular to the load direction when the H-NC cools to T_{amb} whereby an elongation is caused and which is reversed upon melting. Despite the covalent integration of the MNP into the N-NC a higher MNP content causes a decrease of orientation of the crystalline domains resulting in a decreased actuation in the magneto-mechanical experiments.

4. Conclusions

Magnetite nanoparticles (MNP) formed multifunctional covalent netpoints at the nanoscale providing mechanical stability and magnetosensitivity to the H-NC. At 100 °C the MNP contributed significantly to the strength of the hybrid nanocomposites and Young's moduli of up to 5.1 MPa were obtained compared to 2.8 MPa for OPDL networks without MNP. In magneto-mechanical 1W_{mag}-DSE experiments the MNP decreased shape fixity while shape recovery was only slightly increased, however still excellent shape-memory properties ($R_r \geq 95\%$ and $R_f \geq 90\%$) were determined. In magnetically-controlled R_{mag}-DSE the $R_{act,H}$ value was decreased by increasing the wt% of MNP netpoints and a maximum value of 66% for H-NC5 was decreased to 36% for H-NC11. These findings could be related in X-ray scattering experiments to a decreased orientation of the OPDL crystals, which can be attributed on the one hand to an impeding effect of the MNP in crystallization of oriented polymer chain segments and on the other hand to an increase of the crosslink density with increasing MNP content. These results show that in hybrid nanocomposites the performance can be tailored by MNP content, however in terms of their applicability a focus in the direction of mechanical strength or actuation capability needs to be set.

Acknowledgements

The authors would like to thank the Helmholtz Association for funding.

References

1. Behl M, Razzaq MY, and Lendlein A. Advanced Materials 2010;22(31):3388-3410.
2. Baryoseph P, Yaniv G, and Ishai O. Computers & Structures 1987;25(1):11-27.
3. Filho STA. Welding in the World 2011;55(1-2):13-24.
4. Ge Q, Qi HJ, and Dunn ML. Applied Physics Letters 2013;103(13).
5. Eitel W. Zeitschrift Fur Anorganische Und Allgemeine Chemie 1917;100(1/2):95-142.
6. Gunes IS and Jana SC. Journal of Nanoscience and Nanotechnology 2008;8(4):1616-1637.
7. Leng JS, Lan X, Liu YJ, and Du SY. Progress in Materials Science 2011;56(7):1077-1135.

8. Razzaq MY, Behl M, and Lendlein A. Nanoscale 2012;4(20):6181-6195.
9. Meng H and Li GQ. Polymer 2013;54(9):2199-2221.
10. Wu X, Huang W, Zhao Y, Ding Z, Tang C, and Zhang J. Polymers 2013;5(4):1169-1202.
11. Xie T. Polymer 2011;52(22):4985-5000.
12. Agarwal P, Chopra M, and Archer LA. Angewandte Chemie-International Edition 2011;50(37):8670-8673.
13. Xu JW and Song J. Proceedings of the National Academy of Sciences of the United States of America 2010;107(17):7652-7657.
14. Barbucci R, Giani G, Fedi S, Bottari S, and Casolaro M. Acta Biomaterialia 2012;8(12):4244-4252.
15. Dach BI, Rengifo HR, Turro NJ, and Koberstein JT. Macromolecules 2010;43(16):6549-6552.
16. Dell'Erba IE, Hoppe CE, and Williams RJJ. Langmuir 2010;26(3):2042-2049.
17. Jung DH, Jeong HM, and Kim BK. Journal of Materials Chemistry 2010;20(17):3458-3466.
18. Xu JW, Shi WF, and Pang WM. Polymer 2006;47(1):457-465.
19. Razzaq MY, Behl M, Kratz K, and Lendlein A. Advanced Materials 2013;25(40):5730-5733.
20. Chung T, Rorno-Uribe A, and Mather PT. Macromolecules 2008;41(1):184-192.
21. Pandini S, Passera S, Ricco T, Borboni A, Bodini I, Vetturi D, Dassa L, Cambiaghi D, Paderni K, Degli Esposti M, Toselli M, Pilati F, and Messori M. Adaptive, Active and Multifunctional Smart Materials Systems 2013;77:313-318.
22. Westbrook KK, Mather PT, Parakh V, Dunn ML, Ge Q, Lee BM, and Qi HJ. Smart Materials & Structures 2011;20(6).
23. Mandelkern L, Roberts DE, Diorio AF, and Posner AS. Journal of the American Chemical Society 1959;81(16):4148-4157.
24. Oth JFM, Dumitru ET, Spurr OK, and Flory PJ. Journal of the American Chemical Society 1957;79(12):3288-3289.
25. Ge Q, Westbrook KK, Mather PT, Dunn ML, and Qi HJ. Smart Materials and Structures 2013;22(5):055009.
26. Pandini S, Baldi F, Paderni K, Messori M, Toselli M, Pilati F, Gianoncelli A, Brisotto M, Bontempi E, and Ricco T. Polymer 2013;54(16):4253-4265.
27. Sauter T, Heuchel M, Kratz K, and Lendlein A. Polymer Reviews 2013;53(1):6-40.
28. Wagermaier W, Kratz K, Heuchel M, and Lendlein A. Shape-Memory Polymers 2010;226:97-145.
29. Mather PT, Luo XF, and Rousseau IA. Annual Review of Materials Research 2009;39:445-471.
30. Meng QH and Hu JL. Composites Part a-Applied Science and Manufacturing 2009;40(11):1661-1672.
31. Rousseau IA. Polymer Engineering and Science 2008;48(11):2075-2089.
32. Karger-Kocsis J and Keki S. Express Polymer Letters 2014;8(6):397-412.
33. Chen SJ, Hu JL, and Zhuo HT. Composites Science and Technology 2010;70(10):1437-1443.
34. Meng H, Mohamadian H, Stubblefield M, Jerro D, Ibekwe S, Pang S-S, and Li G. Smart Materials and Structures 2013;22(9):093001.
35. Bai S, Zou H, Dietsch H, Simon YC, and Weder C. Macromolecular Chemistry and Physics 2014;215(5):398-404.
36. Li JJ, Rodgers WR, and Xie T. Polymer 2011;52(23):5320-5325.
37. Bothe M and Pretsch T. Macromolecular Chemistry and Physics 2012;213(22):2378-2385.
38. Zhou J, Turner SA, Brosnan SM, Li Q, Carrillo J-MY, Nykypanchuk D, Gang O, Ashby VS, Dobrynin AV, and Sheiko SS. Macromolecules 2014;47(5):1768-1776.
39. Pandini S, Passera S, Messori M, Paderni K, Toselli M, Gianoncelli A, Bontempi E, and Ricco T. Polymer 2012;53(9):1915-1924.
40. Mooney M. J. Appl. Phys. 1940;11(9):582-592.
41. Cui J, Kratz K, Hiebl B, Jung F, and Lendlein A. Tissue Engineering Part A 2011;17(3-4):563-563.

42. Weigel T, Mohr R, and Lendlein A. Smart Materials & Structures 2009;18(2).
43. Mohr R, Kratz K, Weigel T, Lucka-Gabor M, Moneke M, and Lendlein A. Proceedings of the National Academy of Sciences of the United States of America 2006;103(10):3540-3545.
44. Behl M, Zotzmann J, and Lendlein A. International Journal of Artificial Organs 2011;34(2):231-237.
45. Zotzmann J, Behl M, Hofmann D, and Lendlein A. Advanced Materials 2010;22(31):3424-3429.

Graphical abstract:

Magnetically Controlled Shape-Memory Effects of Hybrid Nanocomposites from Oligo(*ω*-pentadecalactone) and covalently integrated magnetite nanoparticles

Muhammad Yasar Razzaq, Ulrich Nöchel, Marc Behl, Andreas Lendlein

Hybrid nanocomposites (H-NCs) with a well-defined nanostructure were prepared from oligo(*ω*-pentadecalactone) (OPDL) coated magnetite nanoparticles (OPDL@MNP), star-shaped trihydroxy terminal OPDL and hexamethylenediisocyanate (HDI). The covalent integration enabled a uniform distribution of the nanoparticles and an increased mechanical strength with an increase of MNP netpoints. H-NCs heated by alternating magnetic field were capable of magnetically controlled one-way and reversible shape-memory effects by cyclic switching of magnetic field on and off.